Materials Research. 2020; 23(6): e20190631
DOI: https://doi.org/10.1590/1980-5373-MR-2019-0631

Microstructure and Corrosion Behavior of Ni-Cr-Mo Nickel-based Alloy Weld

***Yajie Chu*[1,2]*, *Yuan Chen*[1,2], *Yixin Chen*[1,2], *Peng Liu*[3], *Xiaoquan Li*[1,2]**

[1]*Nanjing Institute of Technology, Department of Material engineering, Nanjing 211167, China.*
[2]*Jiangsu Key Laboratory of Advanced Structural Materials and Application Technology, Nanjing, 211167, China*
[3] *Shandong Jianzhu University, School of Materials Science and Engineering, Jinan 250101, China.*

Received: November 14, 2019; Revised: October 28, 2020; Accepted: December 13, 2020

The mechanical properties and corrosion performance of the N10276 alloy welded joint were investigated with nano-hardness testing and electrochemical measurement. The results showed that solidification mode changes from equiaxed crystal to columnar crystal from the center of the weldment to the fusion zone. With the increase of immersion times, the diameter of capacitance arc and the impedance modulus increase, and the corrosion resistance of HAZ decreases. The strengthening effect of welded metal was more obvious than that of heat affected zone for the nickel-based welded joint and especially in coarse grained heat affected zone, the hardening resulted from overheating was not apparent. Nickel-based weld metal with high content of alloying elements were often segregated at interdendritic regions or precipitated in grain interior under nonequilibrium solidification, which differ from conventional low alloy steel welded joint.

Keywords: Nickel-base alloy, Nanoindentation, Corrosion behavior, Electrochemical properties.

1. Introduction

Nickel-based alloy N10276 (wrought Ni-Cr-Mo-W alloy) has been widely used in aerospace, chemical processing, pollution control, nuclear, oil and gas industries because of its excellent corrosion resistance and high temperature mechanical properties[1-3]. In order to improve its corrosion resistance and high temperature strength, the refractory metal elements, Cr, Mo and W were often molten in the alloy. However, high contents of Cr, Mo and W could easily lead to the precipitation of intermetallic compounds (phases) and carbides during air cooling after hot working and/or welding. The precipitates can cause a decrease in corrosion resistance and high temperature mechanical properties. It was proved that three types of secondary phases, TCP μ phase, M_6C carbides and P phase, can appear in alloy N10276 and these second phases are very rich in Cr, Mo and W[4]. The μ phase is hard and brittle, which has a detrimental effect on mechanical properties, especially low temperature tensile[5]. Furthermore, the precipitation of these secondary phases causes the reduction of alloying elements in the γ matrix, which inevitably decreases the corrosion resistance of nickel-based alloy.

It was proved that the corrosion behavior and mechanical properties of the nickel-based alloy were related to thermal cycle processes[6]. During SMAW process, the welded zone and base metal adjacent to welded zone suffered to different thermal cycle processes, so different zones of welded joint would show the different mechanical properties and corrosion behavior. Ramkumar et al.[7] investigated the tungsten inert gas (TIG) welding of Nickel-based metal. Microstructure examination revealed micro-segregation while employing UNS N06022 filler. Due to the prevalence of higher tensile stresses, tensile failures were observed in the weld regions of both the joints irrespective of fillers. But the tensile strength of the welded joints increased while employing low energy laser shock peening. Jaladurgam et al.[8] investigated that hot deformation characteristics and microstructure evolution of Hastelloy C-276. The flow curves confirmed the dynamic recrystallization (DRX) phenomena. Bal et al.[9] showed that effect of post-weld heat treatment on the tensile strength of laser beam welded Nickel-based sheets. It was observed that the samples welded at 60 J/mm failed mainly at the weld zone, while all the samples welded at 120 J/mm failed at the base metal.

Previous investigations mainly concentrated on the hot deformation characteristic[10], precipitation behavior[11], high temperature mechanical properties and corrosion resistance of base metal (N10276)[12]. However, very few studies focused on the microstructure and corrosion performance of the N10276 alloy welded joint (welded zone, heated affected zone, fusion zone and base metal). In fact material corrosion, such as pitting corrosion, is a dynamic damage process. The microstructure and corrosion morphology of welded joint may evolve with time. The microstructure evolution of different zone of welded joint can cause a significant change in the corrosion mechanism and behavior of materials[13-15]. The nickel-based N10276 is often used as an important structure material, and the SMAW method is usually used in nickel-base welded structure. Because the mechanical properties and corrosion resistance are very sensitive to microstructure of welded joint, the research on the joint microstructure evolution is necessary to well understand the corrosion behavior of alloy N10276.

*e-mail: chuyajie@njit.edu.cn

In this paper, the UNS N10276 rolling plate was butt-welded by SMAW. Considering reliable design and optimal production, it is necessary to investigate the effect of welding thermal cycle on the mechanical properties including micro-hardness, surface chemistry, microstructure and corrosion behavior of the nickel-based welded joint.

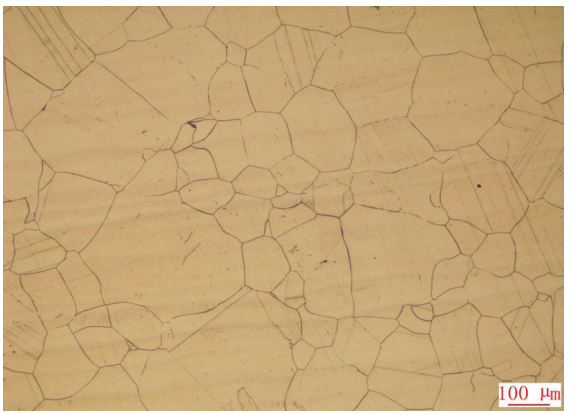

Figure 1. Optical micrograph of as-received alloy UNS N10276.

2. Experimental Procedure

2.1 Materials and welding process

The base metal is a solution heat treatment and over-aged (T7) plate UNS N10276, which was provided by the China Central Iron and Steel Research Institute. The composition of the as-received alloy was given in Table 1[16]. The microstructure of the as-received alloy was shown in Figure 1. It is observed to be austenite equiaxed grains and a small part of annealing twins. The grain size of the base metal is 100um-250um.

The two same base metals (alloy UNS N10276) were butt jointed using the shielded metal arc welding (SMAW) and the selected welding consumable (welding rod) is ENiCrMo-3 (AWS A5.11:2005) with φ3.2mm in diameter. A single "V" type groove with an angle of 60°was prepared on the base metal. The schematic diagram of welded joint is shown in Figure 2, and the welding parameters are listed in Table 2[17,18]. Before welding, the surface of the workpiece was ground with a stainless steel brush to remove the oxide film formed in the air, and then cleaned with acetone to wipe off grease or oils on the surface. A total of 4 weld passes were required to complete the weldment. The interpass

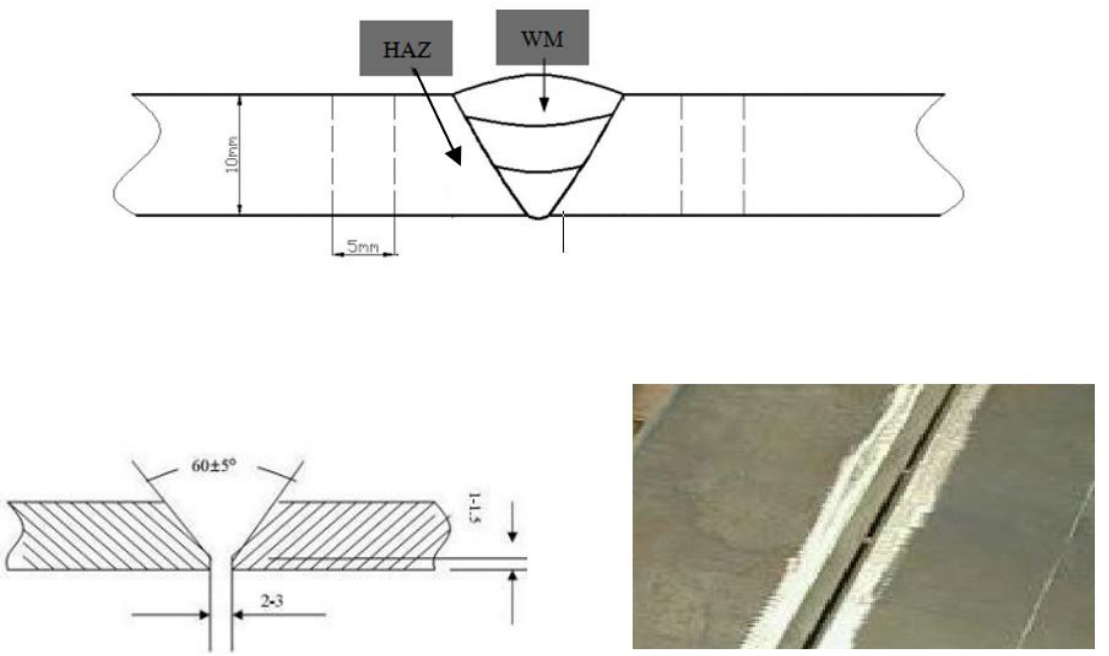

Figure 2. Schematic diagram of the welded joint, welded plate and macrograph.

Table 1. The chemical composition (wt.%) of alloy UNS10276.

Element	Ni	Cr	Mo	W	Fe	Mn	Al	Co	Si	P	V	C
Content(wt%)	Bal.	15.13	15.97	4.14	5.69	0.6	0.54	0.43	0.12	0.05	0.4	0.01

Table 2. Welding parameters during SMAW process.

Weld pass No.	Welding current (A)	Welding voltage (V)	Welding speed (mm/s)	Heat input (W)
1	120	23	3	33120
2	120	23	3	33120
3	120	24	3	34560

temperature is controlled at 423K (150°C). After welding the first layer, the temperature was measured using an infrared thermometer, and when the temperature dropped to 150°C, the second layer was carried out[19].

2.2 Specimen characterization

The surface microstructure and corrosion features of the welded joint were examined by means of optical microscope (OM). Specimens were mounted in epoxy exposed cross-section, and then mechanically ground to 2000grit by a series of abrasive SiC grit sizes, finally polished using 3um diamond suspension. The cross-section of specimens was etched using a mixture of 300ml HCl and 100ml HNO_3 for the OM examination.

Micro-hardness measurements were conducted along the specimen center line at room temperature by holding a test load of 500g for 10s. Micro-hardness values were directly obtained from the tester. The measurement interval in HAZ was fixed at 0.25 mm, while in WZ and BM the distance was 0.5 mm.

A nanoindenter was carried out to measure the nanomechanical properties of the welded joint. The hardness and Young's modulus were calculated from the load-displacement curves using the Oliver and Pharr method[20,21]. Load-displacement curves were gained by nanoindentation tests using an Agilent Technologies Nano Indenter G200. A three-sided pyramidal Berkovich tip with an elastic modulus of 1141 GPa and Poisson's ratio of 0.07 was used for indentations at room temperature. The tests were conducted using a Berkovich tip with a thermal drift lower than 0.05 nm s^{-1} and a strain rate of 0.05 s^{-1}. The maximum load is 150 mN and the Poisson's ratio is 0.289. The loading and unloading rates are 5 $mN \cdot s^{-1}$.

2.3 Electrochemical measurements

Electrochemical measurements were performed via an electrochemical workstation (PARSTAT 2273, Princeton, USA) at room temperature using an aerated 3.5 wt.% NaCl solution, prepared with deionized water. A three-electrode cell setup was employed to characterize the electrochemical response of specimens. The three-electrode system is comprised of a saturated calomel electrode (SCE) as reference electrode, a platinum sheet with 2×2×0.5 mm as a counter electrode and the specimens sectioned from different zones of the butt joint as working electrode. The electrochemical testing specimens were sectioned using a wire-cut electrical discharge machining (WEDM) system according to the schematic diagram of sectioning samples. Specimens for electrochemical testing were mounted in epoxy leaving only 0.8 cm×0.8 cm cross-section area exposed, so the exposed area for testing was 0.64 cm^2. Immediately prior to each testing, the specimens were progressively ground to 2000grit (SiC paper) and then rinsed with acetone, ethanol and deionized water and dried in the air at room temperature. Then, the test specimens were transferred into the test solution before the electrochemical experiment was conducted. The tests for each specimen were conducted at least three times, and the results were averaged. Before each electrochemical experiment, working electrode (specimen for testing) was first cathodically polarized at $-1V_{SCE}$ for 10 min in order to remove the surface oxides formed in the air. Studies have shown that after cathodic polarization, passive films can be reproduced better[22,23].

The test specimens were immersed in the test solution for 60 min to attain a relatively stable value of open-circuit potential (OCP) after cathodic polarization pretreatment. For the potentiodynamic polarization experiment, the test specimens were excited from −1 V towards the anodic direction to +1 V at a scanning rate of 0.5 $mV \cdot s^{-1}$. Electrochemical impedance spectroscopy (EIS) measurements were carried out at OCP after the specimens had been immersed for 1, 8,16, 32 and 48 h, respectively, in a 3.5 wt.% NaCl solution. The testing frequency ranged from 10 kHz to 10 MHz and the AC amplitude was ±10 mV. The data obtained during testing was then fitted using ZSimpWin software.

3. Results and Discussions

3.1 Microstructures

The optical microstructures of the nickel-based alloy welded joint are shown in Figure 3. It can be observed that the nickel-based welded joint is composed of welded zone (WZ), fusion zone (FZ) and heat affected zone (HAZ). The microstructures of different zones are completely dissimilar. The microstructure of WZ consists of fine equiaxed dendrites grains and cellular grains. There are no obvious precipitates in WZ. It is mainly due to the small temperature gradient in the central region of the WZ, which ultimately leads to the formation of equiaxed dendrite grains. Rapid cooling and gas stirring during welding is also beneficial to the formation of fine grain structure in WZ.

As shown in Figure 3c, FZ presents the feature of a coarse cellular structure and columnar crystal and the coarse equiaxed grains were also seen at the HAZ of alloy UNS N10276. Point A in Figure 3c shows the micrograph of the zone near the fusion line and away from the weld center. It mainly consists of columnar dendrite structure. There are two main reasons for the columnar crystal, one is the fact that thermal gradients in point A zone are steeper than in welded zone center and the other is the decrease of non-spontaneity nucleation sites due to the serious burning of alloy elements. The steeper thermal gradients in fusion zone are beneficial to the growth of columnar dendritic crystals. It can be seen from Figure 3b that from the center of WZ to the fusion zone, the solidification mode changes from equiaxed dendrites crystal to columnar crystal.

The microstructure of HAZ grows and element serious segregation appears in grain boundary due to the thermal cycle during welding. Many researchers have studied the element segregation and precipitation behavior of the nickel-based alloy. Pu et al.[16] studied the types of phases and phase fraction in the alloy UNS N10276 by Thermo-Calc software calculation. There may be μ phase, σ phase, M_6C and $M_{23}C_6$ in the temperature range of 500 °C to 1130 °C. However, μ phase is the main precipitated particles in the sensitive temperature range.

3.2 Mechanical properties

Figure 4 shows indenting locations on the surface of the micro-indentation sample. Micro-hardness measurements

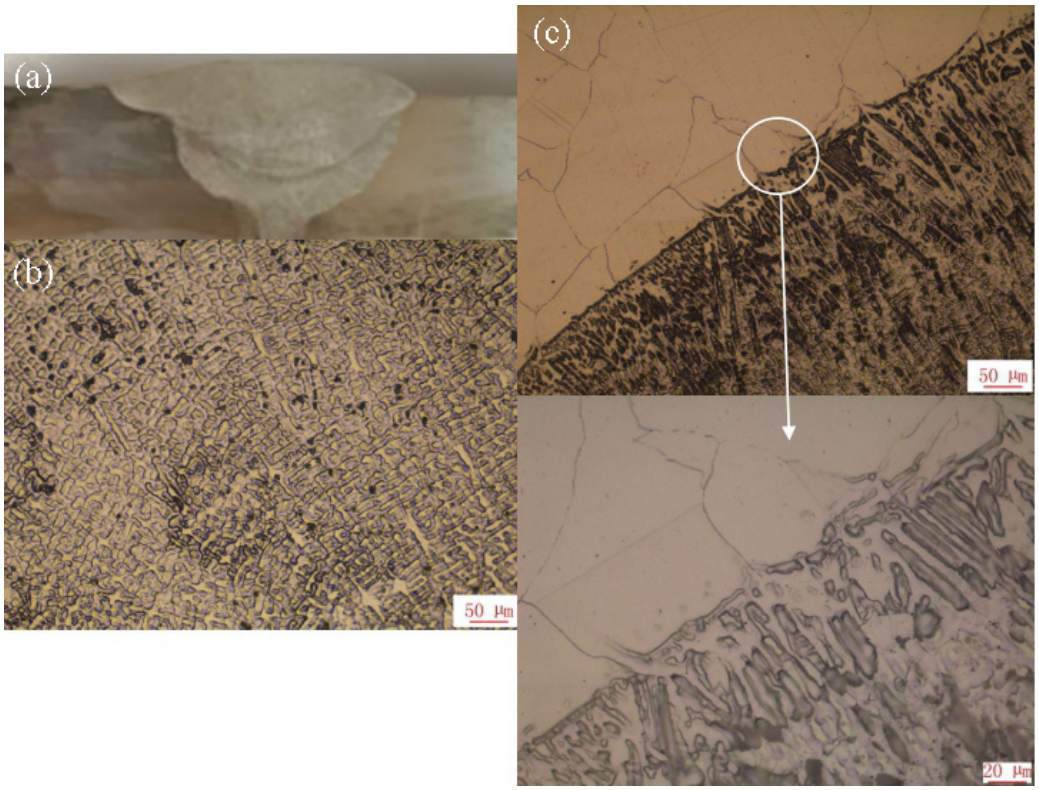

Figure 3. Micrograph of welded joint. (a) welded zone; (b) HAZ; (c) Fusion zone.

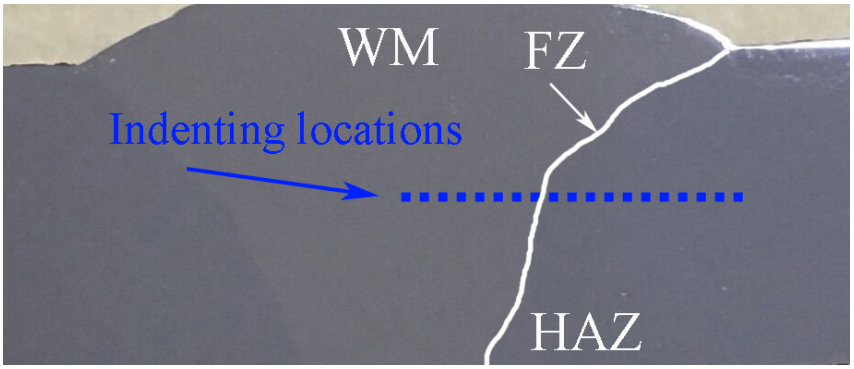

Figure 4. Indentation sample surface after indenting locations.

were conducted on the cross-section of welded joint, in order to determine the hardness at different zone (BM, HAZ and WZ). Figure 5 presents the hardness values at different zone of welded joint. It can be seen that micro-hardness in the cross-section of welded joint shows a decrease first and then increase from the BM zone to WZ. The hardness value at WZ is smaller than that at BM zone and HAZ. The average micro-hardness at WZ is 210 HV, and peak micro-hardness at WZ is as high as 220 HV. The hardness at HAZ is higher than that at BM zone and WZ. The highest hardness value is 367 HV, which is observed in the HAZ. In HAZ, hardness is gradually reduced to the level of BM. A rapid decrease of the hardness value can be observed near the fusion lines when the test location is transferred to WZ.

Higher hardness results in lower plasticity and high temperature properties. Pandey and Mahapatra[24] and Pandey et al.[25]. studied the mechanical properties of P91 steel weld metal and heat affected zone (HAZ). However, in the case of welded joints of such steels, the presence of HAZ can cause the joint to have lower creep strength than the base metal because of the poorer plasticity and elasticity.

The load on sample-displacement into surface curves(P-h) measured in the WZ, FZ, HAZ, and BM regions are presented in Figure 6. For clarity, only one typical curve obtained as the average of the data from three indentations in each region is shown in this figure. This indicates that for the present weld zone, the indentation response is reliable. As shown in Figure 6, a common characteristic of the five curves is that the indentation depths increase rapidly with the increasing

load at the initial period, then remains unchanged, and finally drops down. This can be explained easily that elastic deformation was prior to plastic deformation. With the increase of loading, the reason why the rate of increasing depth drops is that the depth of indentation is largely affected by work hardening, and work hardening becomes more and more serious with the increase of depth during loading. But the maximum indentation depth and the shape of P-h curves have a significant variation exit between those in different regions. Under the same maximum load, the indentation depth in the WZ is the largest, while which in the CGHAZ is the smallest, and the indentation depth in the BM and the FZ is also different. This difference is consistent with the trend of micro-hardness, and also indirectly reflects the difference in hardness of the welded joint.

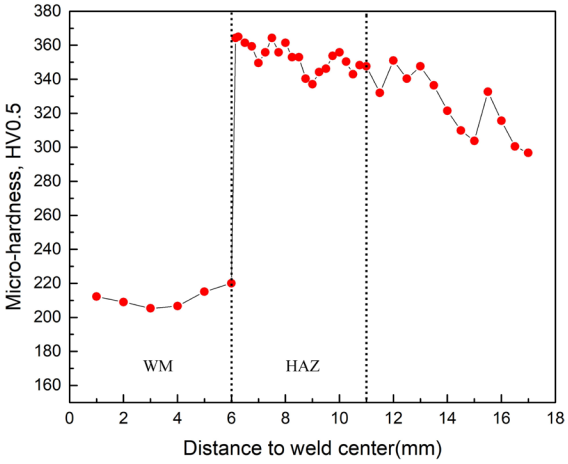

Figure 5. Micro-hardness distribution along the centerline of in the SMAW welding joint.

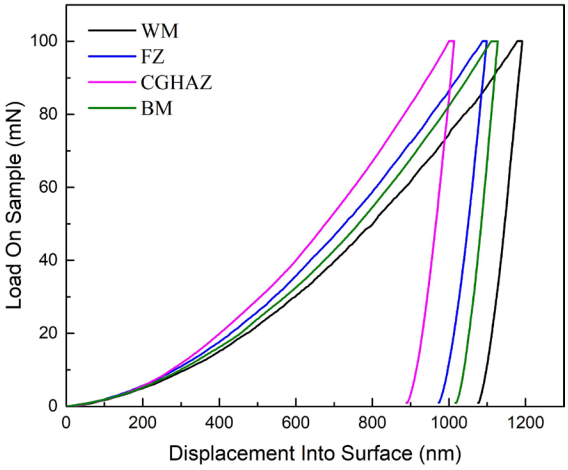

Figure 6. Typical indentation P-h curves in the nickel-based welded joint (a constant loading and unloading rate of 5 $mN \cdot s^{-1}$).

The nano-hardness and elasticity modulus measured in various regions are shown in Figure 7. Both nano-hardness and elasticity modulus change significantly in different regions. As shown in Figure 7a, the distribution of hardness appears obvious regularity which shows the nano-hardness value of HAZ is highest and FZ is lowest. The high hardness in HAZ is in agreement with micro-hardness distribution of welded joint (Figure 5). The nanohardness value of the HAZ is about 1GPa larger than the FZ. The reason why the HAZ has the highest nano-hardness is the coarse lath martensite produced under the thermal cycle of welding. The high hardness of lath martensite makes the nano-hardness of the HAZ increase and the toughness decreases, and the fast cooling speed and high dislocation density of HAZ make it become the weakest link in fatigue and other properties of the joint. It can be seen that alloy N10276 contains more Cr, Mo and W elements by the EDS analysis (Table 1), which causes solid solution hardening and aging precipitation hardening. Additionally, the eutectoids, which is rich in Mo and W, could act as dispersion and hinder the movement of the dislocations. The distributions of elastic modulus across the weld zone are presented in Figure 7b with the same illustrated way as Figure 7a. It is interesting to note in Figure 7b that the elastic modulus of FZ is still the lowest, but the BM is the highest, not HAZ. In other words, the elasticity modulus values in the HAZ region gradually decrease from the BM to the FZ region. The smaller elasticity modulus makes the fusion zone less resistant to deformation.

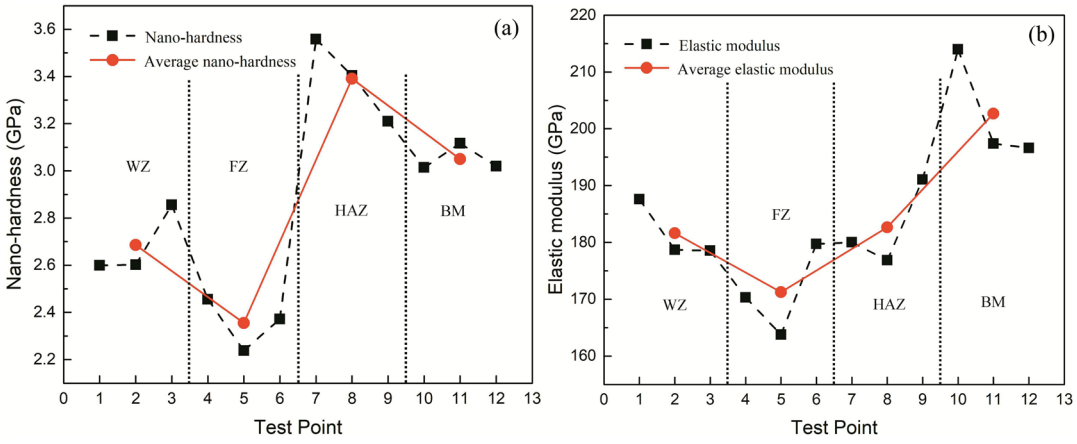

Figure 7. Nanoindentation test results of welded joints. (a) Distributions of nano-hardness across the weld zone. (b) Distributions of elastic modulus across the weld zone.

3.3 Corrosion behavior

From the above results discussed, the microstructures in BM zone, HAZ, FZ and WZ of nickel-based welded zone are very different, and different microstructures may determine different corrosion resistance. It has been reported that many influencing factors such as microstructure, grain size, alloy composition, phases and precipitation, oxide/passive film, residual stress, temperature and corrosion environment, etc., may affect the corrosion behavior of alloys[26,27]. The aim of electrochemical investigation was to obtain some information so as to ascertain how welding processes influence the pitting corrosion behavior of nickel-based welded joint in a 3.5 wt.% NaCl solution.

D.K. Dwivedi[28,29] studied corrosion behavior of the A-TIG welded SS409 weld fusion zone. The maximum corrosion potential (Ecorr) was shown by the weld made using a welding current of 215 A and a welding speed of 95 mm/min. The minimum Ecorr was observed in the weld made using a welding current of 190 A and a welding speed of 120 mm/min. It can be seen that welding process parameters have great influence on corrosion behavior. D.K. Dwivedi also studied corrosion behavior of AA2014 aluminium alloy friction stir welding. It showed that higher tool rotation speed and lower welding speed were more susceptible to the corrosion of welded joint, but the inhomogeneity of the welded joint leads to a decrease in the corrosion resistance of the weld. And the coarse precipitates also affected the corrosion performance.

In order to better analyze the effects of thermal cycle during welding on pitting corrosion resistance, this part was accomplished by using EIS and cyclic polarization measurements. It should be noted that because the width of FZ is very small (0.06~0.22mm) (Figure 1d), it is difficult to evaluate independently the corrosion resistance of microstructure in FZ. Therefore, the corrosion resistance of microstructure in FZ will not be evaluated, and only that of BM, HAZ and WZ was discussed.

In order to investigate deeply electrochemical properties of oxide films formed on the surface of the nickel-based welded joint, EIS measurements were carried out at OCP after 1, 6, 24, and 72h immersion in a 3.5 wt.% NaCl solution at room temperature. The EIS diagrams of the BM, HAZ and WZ of the welded joint are shown in Figure 8-10. The fitted impedance parameters obtained for all specimens are summarized in Table 3.

The EIS diagrams of WZ, BM, HAZ specimen shows similar features in a 3.5%NaCl solution for different times. From the Nyquist plots, it can be seen that there is only capacitance arc at high frequency for all immersion times. With the increase of immersion times, the diameter of capacitance arc increased.

Figure 8 shows the EIS diagrams of the WZ zone in a 3.5 wt.% NaCl solution. The Nyquist plots showed a large semicircle at low frequency and one small semicircle at high frequency. The Bode diagrams showed two peaks in the high–medium frequency range and the medium–low frequency range, respectively. It can be seen that with the

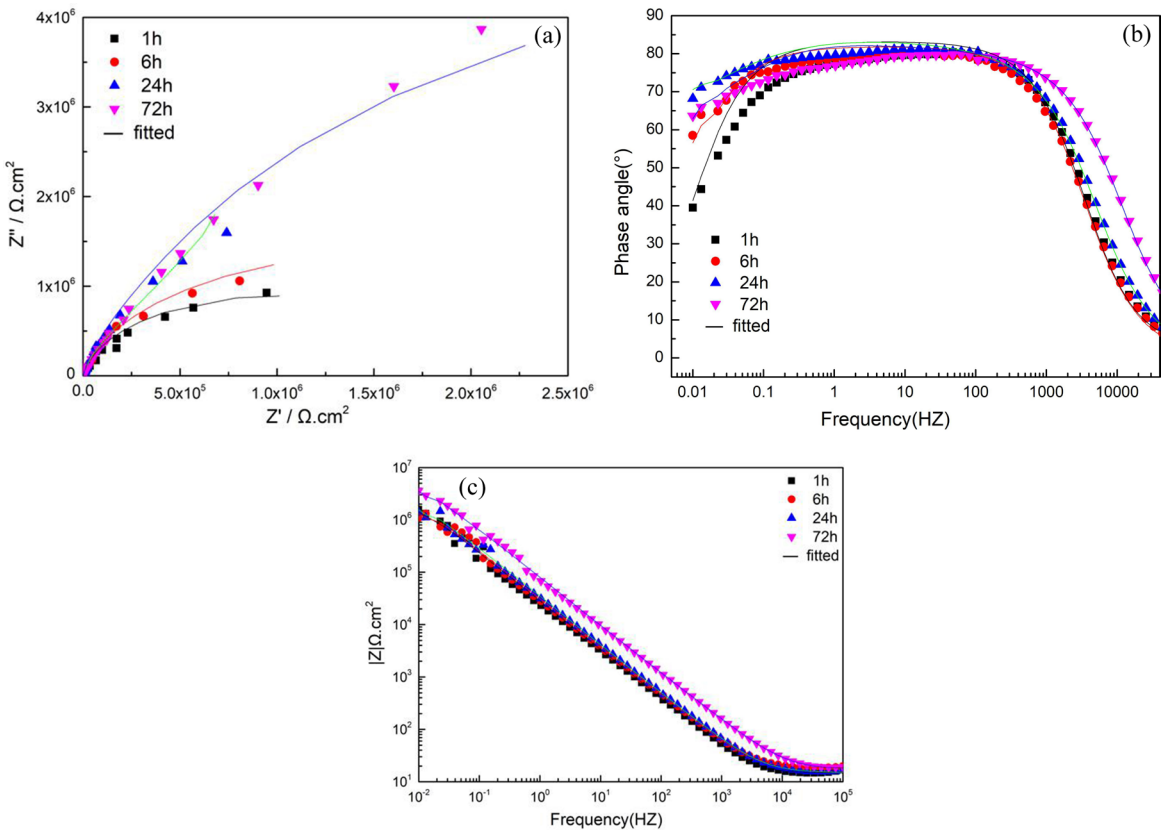

Figure 8. EIS spectra measured at OCP after immersion for different times in a 3.5% NaCl at room temperature for WZ specimen.

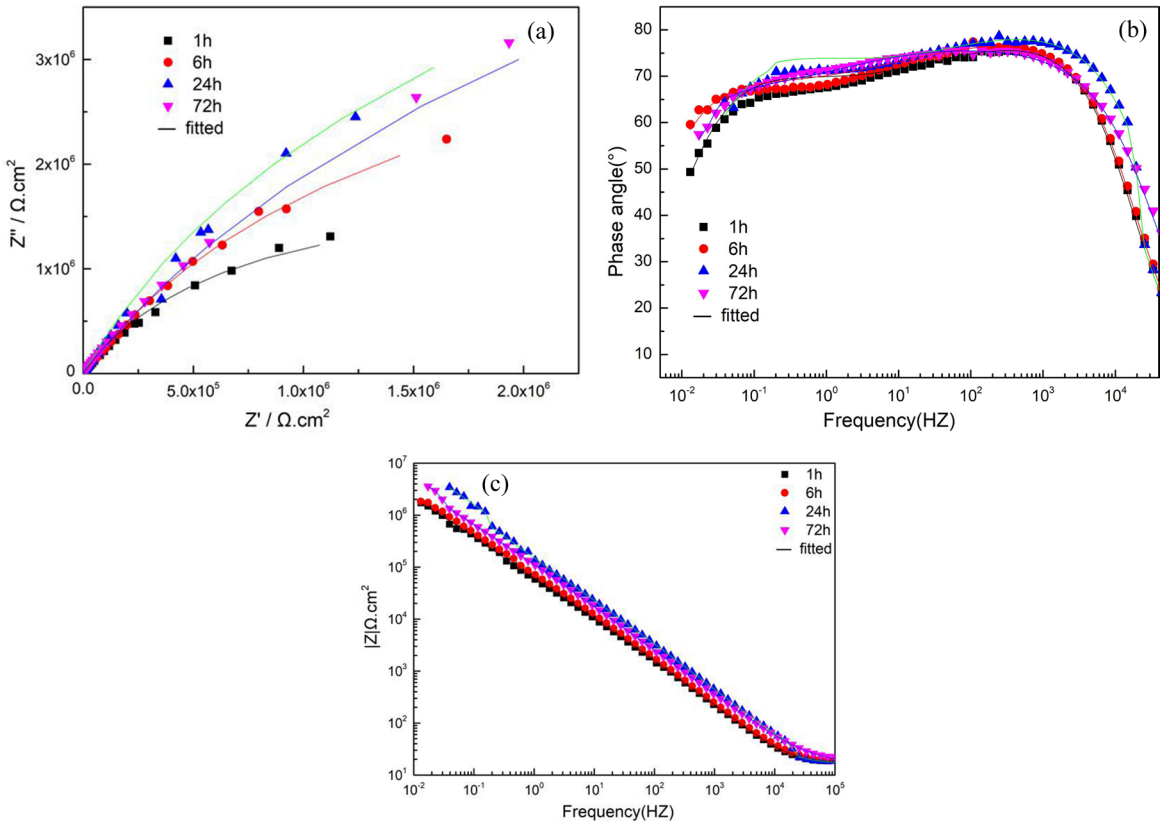

Figure 9. EIS spectra measured at OCP after immersion for different times in a 3.5% NaCl at room temperature for BM specimen.

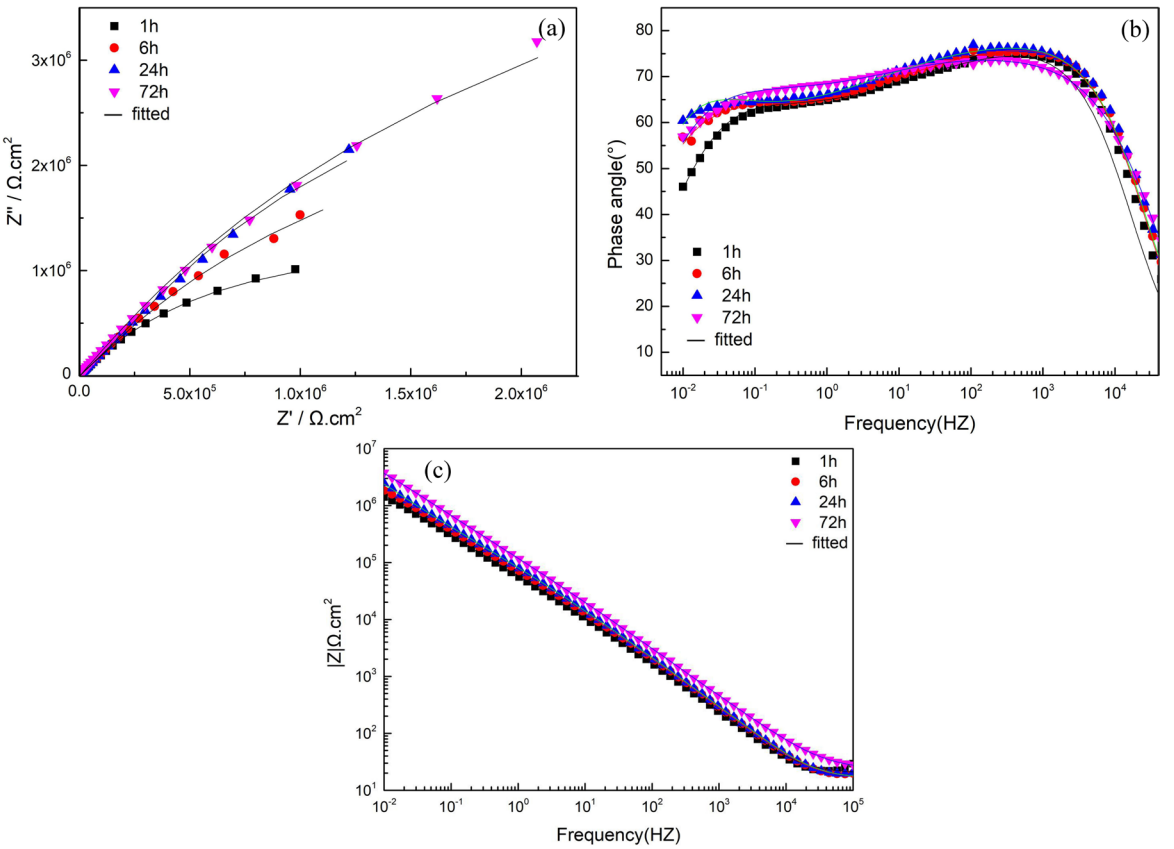

Figure 10. EIS spectra measured at OCP after immersion for different times in a 3.5% NaCl at room temperature for HAZ specimen.

Table 3. Fitted EIS results for BM, HAZ and WZ specimens measured at OCP

Specimen	R_s	R_1	Q_1	n_1	Y_w	R_2	Q_2	n_2
	($\Omega.cm^2$)	($\Omega.cm^2$)	(F/cm^2)		($\Omega^{-1}.s^{-0.5}$)	($\Omega.cm^2$)	(F/cm^2)	
BM-1h	18	1.50×10^3	5.59×10^{-6}	0.82	9.70×10^{-5}	2.55×10^6	9.11×10^{-6}	0.88
BM-6h	18	1.36×10^3	5.90×10^{-6}	0.61	1.45×10^{-5}	3.35×10^6	7.39×10^{-6}	0.91
BM-24h	17	1.37×10^3	5.90×10^{-6}	0.81	1.40×10^{-6}	3.50×10^6	5.12×10^{-6}	0.87
BM-72h	17	2.02×10^3	3.50×10^{-6}	0.84	5.16×10^{-5}	5.40×10^6	4.70×10^{-6}	0.89
HAZ-1h	16	1.40×10^2	3.54×10^{-6}	0.86	1.45×10^{-5}	1.01×10^5	5.81×10^{-6}	0.92
HAZ-6h	17	1.03×10^2	2.64×10^{-6}	0.87	5.96×10^{-6}	1.08×10^5	5.04×10^{-6}	0.89
HAZ-24h	16	1.80×10^2	3.49×10^{-6}	0.86	2.69×10^{-5}	1.12×10^5	3.09×10^{-6}	0.90
HAZ-72h	17	1.80×10^2	3.12×10^{-6}	0.81	7.27×10^{-6}	1.14×10^5	2.72×10^{-6}	0.97
WZ-1h	19	3.02×10^2	1.99×10^{-6}	0.88	7.60×10^{-6}	1.81×10^6	6.40×10^{-6}	0.89
WZ-6h	16	3.10×10^3	1.66×10^{-6}	0.86	5.70×10^{-6}	2.09×10^6	4.10×10^{-6}	0.90
WZ-24h	16	3.90×10^2	1.40×10^{-6}	0.87	3.20×10^{-6}	2.16×10^6	2.10×10^{-6}	0.89
WZ-72h	19	4.30×10^2	1.09×10^{-6}	0.89	1.90×10^{-6}	2.12×10^6	2.13×10^{-6}	0.81

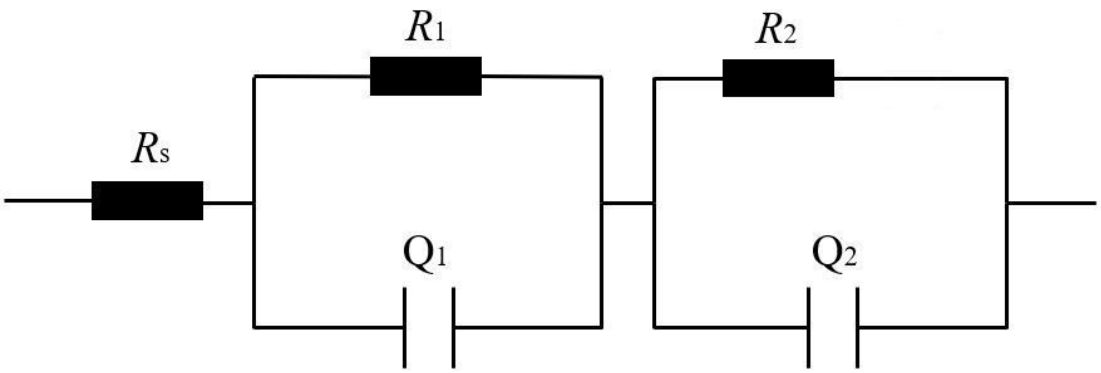

Figure 11. Equivalent electronic circuit for fitting impedance.

increase of immersion time, the impedance modulus in the medium–low frequency range increases but the impedance diagrams are very similar because of the stable films. For the BM and HAZ zone, the impedance diagrams show the same features in comparison with the WZ zone, as indicated in Figure 9 and 10. Two time constants are generally considered to be the response of a passive film consisting of a compact inner layer and a porous outer layer. The previous studies have shown that the passive films on nickel-base alloys can be more described as a double layer structure composed of an n-type outer region containing Ni/Fe oxide and a p-type inner region containing Cr oxide[28,29]. The low frequency time constant has been related to the inner barrier layer, and the time constant at high frequency range has been associated to the porous outer layer.

The equivalent electrical for passive films is shown in Figure 11. In this model, Rs corresponds to the resistance of solution. R1 and Q1 correspond to the resistance and capacitance of the outer layer, respectively. R2 and Q2 correspond to the resistance and capacitance of the inner layer[30,31]. In general, an ideal capacitor (Q) is replaced with a constant phase element (CPE) because of surface roughness and dislocations, etc.

Table 3. shows the fitted impedance parameters. It can be seen that the value of n_1 and n_2 are very similar and almost independent of immerse time. The value of Q_1 and Q_2 decrease with the increase of immerse time, indicating the change of the passive film. From the Table 3, it can be seen that the value of is R_2 much higher than the value of R_1, which indicates that the barrier layer play an important role in the protection of the passive film. The lower R_1 value of may be attribute to the dissolution of Ni and Fe, which lead to the out layer oxide film with more defects.

The R_2 values of BM and WZ specimens are higher than that of HAZ specimens at all immersion times, which indicates that the barrier layers formed on the surface of BM and WZ specimens show more protective than that formed on the HAZ specimens. It is known that polarization resistance R_p is equal to the sum of R_1 and R_2. Because the value of R_2 is much higher than the value of R_1, the value of R_p can be represented the value of R_2. As a result, the corrosion resistance of HAZ decreases after Ni-base alloy N10276 is welded.

Conclusion

This study performs comprehensive Nanoindentation, micro-hardness, optical microscopy characterization, as well as electrochemical measurement, of the BM, HAZ, FZ and WZ, of a N10276 alloy welded joint. The study then develops a equivalent electrical model in all three regions of the welded joint. Key conclusions are summarized as follows:

1. Microstructure of WZ consists of fine equiaxed dendrites grains and cellular grains. FZ presents the feature of a coarse cellular structure and columnar

crystal. From the center of WZ to the fusion zone, the solidification mode changes from equiaxed dendrites crystal to columnar crystal.

2. The higher dislocation density caused by the higher cooling rate lead to the hardness the HAZ are the largest and the hardness of BM is second only to it. The hardnessin is in agreement with micro-hardness distribution of welded joint.
3. With the increase of immersion times, both the diameter of capacitance arc and the impedance modulus increased and the corrosion resistance of HAZ decreases after Ni-base alloy N10276 is welded.
4. The barrier layers formed on the surface of BM and WZ specimens show more protective than that formed on the HAZ specimens and the corrosion resistance of HAZ decreases after Ni-base alloy N10276 is welded.

4. Acknowledgments

The authors acknowledge financial support provided by the Primary Research & Developement Plan of Jiangsu Province (BE2017168).

5. References

1. Ahmad M, Akhter JI, Akhtar M, Iqbal M, Ahmed E, Choudhry MA. Microstructure and hardness studies of the electron beam welded zone of Hastelloy C-276. J Alloys Compd. 2005;390(1-2):88. http://dx.doi.org/10.1016/j.jallcom.2004.08.031.
2. Mehta KK, Mukhopadhyay P, Mandal R, Singh A. Mechanical properties anisotropy of cold-rolled and solution-annealed Ni-based Hastelloy C-276 alloy. Metall Mater Trans, A Phys Metall Mater Sci. 2014;45(8):3493-504.
3. Pu EX, Zheng WJ, Song ZG, Feng H, Yang F, Dong H. Effects of temperature and strain rate on tensile deformation behavior of superalloy UNS N10276. Mater Sci Eng A. 2017;699:88-98.
4. Rocha AMF, Bastos AC, Cardoso JP, Rodrigues F, Fernandes CM, Soares E, et al.. Corrosion behaviour of WC hardmetals with nickel-based binders. Corros Sci. 2019;147(6):384-93.
5. Yao J, Zhang J, Wu G, Wang L, Zhang Q, Liu R. Microstructure and wear resistance of laser cladded composite coatings prepared from pre-alloyed WC-NiCrMo powder with different laser spots. Opt Laser Technol. 2018;101(3):520-30.
6. Kong Y, Chang P, Li Q, Xie L, Zhu S. Hot deformation characteristics and processing map of nickel-based C276 superalloy. J Alloys Compd. 2015;622:738-44.
7. Ramkumar KD, Narenthiran A, Konjenti A, Pravin PN, Kanish TC. Effect of low energy laser shock peening on the mechanical integrity of Hastelloy C-276 welds. J Mater Process Technol. 2019;274:116296. http://dx.doi.org/10.1016/j.jmatprotec.2019.116296.
8. Jaladurgam NR, Kanjarla AK. Hot deformation characteristics and microstructure evolution of Hastelloy C-276. Mater Sci Eng A. 2018;712:240-54. http://dx.doi.org/10.1016/j.msea.2017.11.056.
9. Bal KS, Majumdar JD, Choudhury AR. Effect of post-weld heat treatment on the tensile strength of laser beam welded Hastelloy C-276 sheets at different heat inputs. J Manuf Process. 2019;37:578-94.
10. Yang L, Zhu G, Dong J, Zhang M. Hot deformation characteristics and forging process of corrosion resistant nickel-base C-276 alloy. Procedia Eng. 2012;27:1008-15.
11. Leonard RB. Thermal stability of hastelloy alloy C-276. Corrosion. 1969;25(5):222-32.
12. Li Z, Han J, Lu J, Chen J. Cavitation erosion behavior of Hastelloy C-276 nickel-based alloy. J Alloys Compd. 2015;619:754-9.
13. Park MC, Shin GS, Yun JY, Heo JH, Kim DI, Kim SJ. Damage mechanism of cavitation erosion in austenite→martensite phase transformable Fe-Cr-C-Mn/Ni alloys. Wear. 2014;310(1-2):27-32.
14. Stella J, Poirier T, Pohl M. Cavitation-erosion of 3Y-TZPs obtained at different sintering temperatures. Wear. 2013;300(1-2):163-8.
15. Wang Z, Zhu J. Correlation of martensitic transformation and surface mechanical behavior with cavitation erosion resistance for some iron-based alloys. Wear. 2004;256(11-12):1208-13.
16. Pu E, Zheng W, Song Z, Zhang K, Yang F, Lu H, et al. Evolution of microstructure and tensile properties during solution treatment of nickel-based UNS N10276 alloy. Mater Sci Eng A. 2017;705:335-47.
17. Pandey C, Giri A, Mahapatra MM. On the prediction of effect of direction of welding on bead geometry and residual deformation of double-sided fillet welds. Int J Steel Struct. 2016;16(2):333-45.
18. Narang HK, Mahapatra MM, Jha PK, Sridhar PVSS, Biswas P. Experimental and numerical study on effect of weld reinforcement on angular distortion of SAW square butt welded plates. J Weldi Join. 2018;36(2):48-59.
19. Manikandan M, Danny Raj A, Sathish Kumar M, et al. Investigation on microstructure, micro segregation and mechanical properties of ATIG welded Alloy C-276. Mater Today Proc. 2018;5:6702-10.
20. Zhang Q, Tang R, Yin KJ, Luo X, Zhang L. Corrosion behavior of Hastelloy C-276 in supercritical water. Corros Sci. 2009;51(9):2092-7.
21. Ma Y, Lu DG, Mao XP, Zhang LY, Cai J. Microstructure analysis of stress rupture performance of hastelloy C-276 alloy at 650 °C. Rare Met Mater Eng. 2010;39(9):1571-4.
22. Jin SX, Guo LP, Yang DJ, Fu DJ, Liu CS, Xiao W, et al. Microstructural evolution in nickel alloy C-276 after Ar + ion irradiation. Nucl Instrum Methods Phys Res B. 2011;269(3):209-15.
23. Hay J, Agee P, Herbert E. Continuous stiffness measurement during instrumented indentation testing. Exp Tech. 2010;34(3):86-94.
24. Pandey C, Mahapatra MM. Effect of groove design and post-weld heat treatment on microstructure and mechanical properties of P91 steel weld. J Mater Eng Perform. 2016;25(7):2761.
25. Pandey C, Giri A, Mahapatra MM, Kumar P. Characterization of microstructure of HAZs in as-welded and service condition of P91 pipe weldments. Met Mater Int. 2017;23(1):148-62.
26. Chui P, Sun K, Sun C, Yang X, Shan T. Effect of surface nanocystallization induced by fast multiple rotation rolling on hardness and corrosion behavior of 316L stainless steel. Appl Surf Sci. 2011;257(15):6787-91.
27. Barranco V, Onofre E, Escudero ML, García-Alonso MC. Characterization of roughness and pitting corrosion of surfaces modified by blasting and thermal oxidation. Surf Coat Tech. 2010;204(23):3783-93.
28. Vidyarthy RS, Dwivedi DK. Analysis of the corrosion behavior of an A-TIG welded SS 409 weld fusion zone. J Mater Eng Perform. 2017;26(11):5375-84.
29. Sinhmar S, Dwivedi DK. Effect of weld thermal cycle on metallurgical and corrosion behavior of friction stir weld joint of AA2014 aluminium alloy. J Manuf Process. 2019;37:305-20.
30. Rondelli G, Torricelli P, Fini M, et al. In vitro corrosion study by EIS of a nickel-free stainless steel for orthopaedic applications. Biomaterials. 2005;26(7):739-44.
31. Kocijan A, Merl DK, Jenko M. The corrosion behaviour of austenitic and duplex stainless steels in artificial saliva with the addition of fluoride. Corros Sci. 2011;53(2):776.